ACS APPLIED MATERIALS & INTERFACES

www.acsami.org

Research Article

Mechanistic Insights into the Interplay between Ion Intercalation and Water Electrolysis in Aqueous Batteries

Yuxin Zhang, Chunguang Kuai, Anyang Hu, Lu Ma, Sha Tan, Inhui Hwang, Linqin Mu, Muhammad Mominur Rahman, Cheng-Jun Sun, Luxi Li, Enyuan Hu, and Feng Lin*

Cite This: *ACS Appl. Mater. Interfaces* 2022, 14, 12130–12139

Read Online

ACCESS | Metrics & More | Article Recommendations | Supporting Information

ABSTRACT: Improving electrolyte stability to suppress water electrolysis represents a basic principle for designing aqueous batteries. Herein, we investigate counterintuitive roles that water electrolysis plays in regulating intercalation chemistry. Using the $Na_xFe[Fe(CN)_6]||NaTi_2(PO_4)_3$ ($x < 1$) aqueous battery as a platform, we report that high-voltage overcharging can serve as an electrochemical activation approach to achieving concurrent Na-ion intercalation and an electrolytic oxygen evolution reaction. When the cell capacity is intrinsically limited by deficient cyclable Na ions, the electrolytic water oxidation on the cathode allows for extra Na-ion intercalation from the electrolyte to the $NaTi_2(PO_4)_3$ anode, leading to a major increase in cyclable Na ions and specific capacity. The parasitic oxygen generation and potential transition-metal dissolution, as proved by our synchrotron and imaging tools, can be significantly mitigated with a simple reassembling approach, which enables stable electrochemical performance and sheds light on manipulating ion intercalation and water electrolysis for battery fast charging and recycling.

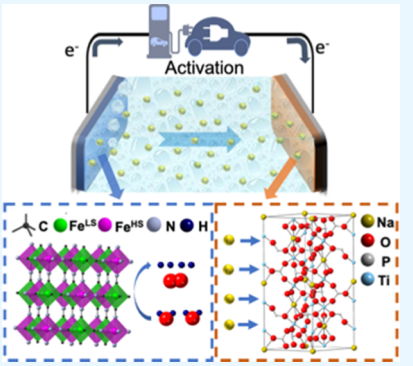

KEYWORDS: *aqueous battery, ion intercalation, electrolytic reaction, electrochemical activation, fast charging*

INTRODUCTION

Na-ion batteries have been considered as a potential alternative to Li-ion batteries for some applications such as grid storage.[1−3] Similar to Li-ion batteries, flammable Na-ion organic electrolytes also pose considerable safety concerns over Na-ion batteries. Aqueous Na-ion batteries (ASIB), which utilize water-based electrolytes, can eliminate the potential hazard of cell explosion and reduce electrolyte toxicity.[4,5] However, constructing a sustainable, high-energy ASIB with a two-electrode, rocking-chair cell configuration has been challenging, arising from technical barriers in identifying a compatible electrode−electrolyte system.

Owing to its narrow electrochemical stability window (1.23 V vs standard hydrogen electrode (SHE)),[6] water in aqueous electrolytes can be readily electrolyzed through oxygen evolution reaction (OER) on the positive electrode when the applied voltage exceeds the water oxidation potential. As a result, the regions near the electrode surface become more acidic, which can chemically degrade electrode materials. Furthermore, oxygen molecules can react with the reduced anode (Na-ion intercalated), thus reducing energy efficiency and causing irreversible capacity loss.[7] Many efforts have been devoted to expanding the voltage window of aqueous electrolytes to enhance the output energy without introducing OER.[4,8,9] For example, the development of "water-in-salt" Na-ion electrolytes, through reducing free water molecules and enhancing cation−anion associations, enables an enlarged voltage stability window of 2.5 V for the 9.26 m sodium trifluoromethane sulfonate (NaOTF) aqueous electrolyte and achieves a stable output specific energy of 31 Wh/kg at 0.2C for a $Na_{0.66}[Mn_{0.66}Ti_{0.34}]O_2||NaTi_2(PO_4)_3$ (NTP) battery.[4] Similarly, other Na salts with high solubility in water, such as sodium perchloride ($NaClO_4$),[6,8,10] sodium trifluoromethanesulfonimide (NaTFSI), and sodium bis(fluorosulfonyl)imide (NaFSI),[5,11,12] have also been used to formulate water-in-salt Na-ion electrolytes to suppress the electrolytic water decomposition in ASIB. In addition to the novel design of the electrolytes themselves, other strategies have been reported to stabilize the utilized electrolyte in aqueous devices, such as adopting asymmetric device configuration,[13,14] synthesizing suitable electrode materials with high OER potential,[15−17] etc. With these approaches, the stability window can be further enlarged to 2.6 V.[18] Therefore, avoiding water electrolysis has been a norm for determining the upper cutoff voltage and obtaining stable performance in aqueous batteries.

Managing the cathode−anode crosstalk, especially maintaining cyclable ion inventory, is another technical challenge in developing rechargeable batteries with a two-electrode, rocking-chair cell configuration. For example, the Li-ion inventory

Received: October 12, 2021
Accepted: February 15, 2022
Published: March 1, 2022

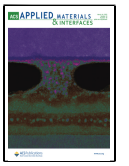

https://doi.org/10.1021/acsami.1c19684
ACS Appl. Mater. Interfaces 2022, 14, 12130−12139

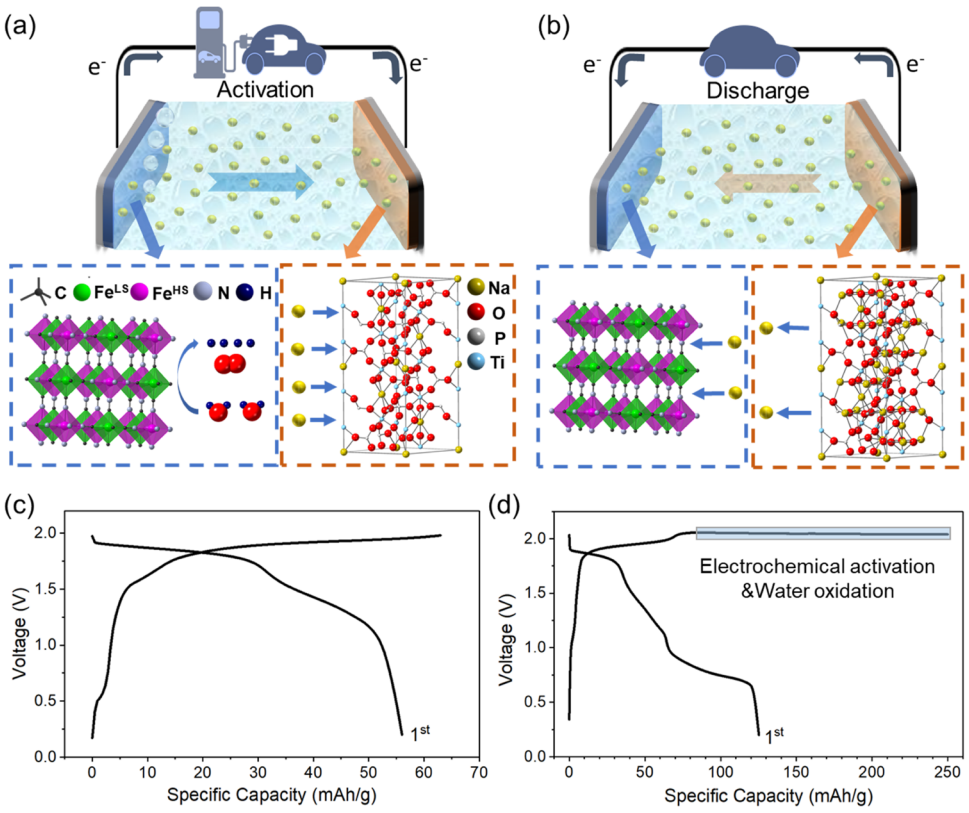

Figure 1. Reaction scheme and performance of NaFeHCF||NTP full cell with electrochemical activation. (a) Scheme of redox reactions on both electrodes upon electrochemical activation. A light blue arrow suggests the direction of Na-ion transport. The content in the blue dashed frame indicates that electrolytic water oxidation occurs on the NaFeHCF cathode surface, while the yellow dashed frame shows that Na ions in the electrolyte intercalate into NTP anode. (b) Scheme of redox reactions on both electrodes upon discharging. The excess Na ions induced by extra ion intercalation in the NTP anode are extracted and inserted into the cathode during discharging, resulting in the enriched Na-ion storage in the fully discharged NaFeHCF cathode compared to the pristine material. (c) First charge−discharge curve of the NaFeHCF||NTP full cell without electrochemical activation in the first charge. The voltage window is 0.2−2 V, and the current rate applied to the cell is 1C (170 mA/g-cathode). Such cell exhibits inferior specific discharge capacity of 56 mAh/g. (d) First charge−discharge curve of the NaFeHCF||NTP full cell with electrochemical activation in the first charge. The cell is overcharged to 250 mAh/g upon the first cycle, and a normal charging protocol (0.2−2 V) is applied to the following cycles. Such cell exhibits a superior specific capacity of 124 mAh/g. The specific capacity is calculated based on the mass of the active cathode.

loss has been identified to be the primary aging mechanism in commercial Li-ion batteries due to the surface layer growth, electrolyte decomposition, and dendrite formation.[19,20] Similarly, to achieve high specific capacity and stable output energy density in ASIBs, sufficient ion intercalation enabled by rich Na-ion inventory is desired. However, some cathode candidates for ASIBs suffer from poor Na-ion storage owing to the intrinsic defects, leading to inferior capacity in the full-cell configuration. For example, Prussian blue ($Na_xTM[Fe(CN)_6]_y$, PB) materials are promising cathodes for ASIBs due to their excellent stability against water and rapid ion transport kinetics.[10,21−23] Nevertheless, PB materials usually have a high $[Fe(CN)_6]^{4-}$ vacancy concentration and tend to have Fe in its Fe^{3+} form, which inevitably leads to Na-ion deficiency due to the charge compensation need, resulting in low reversible capacity.[21,24] Recent studies focus on the chemical synthesis procedure and have reported the preparation of Na-rich PB cathodes by controlling reaction temperature and modulating precursors in the PB synthesis,[21,25,26] which enables high specific capacity in the full cell configuration.[10,21,27] Therefore, increasing the concentration of cyclable Na ions to maximize ion intercalation is ubiquitously important in full cell ASIBs.

Although electrolytic reaction and ion-intercalation reaction are the key factors influencing the electrochemical performance of ASIBs, there is still a lack of understanding about the interplay between these reactions and their synergistic impacts on battery performance. In this work, we aim to investigate the relationship between the ion intercalation and electrolytic processes in the platform $Na_xFe[Fe(CN)_6]||NaTi_2(PO_4)_3$ ($x < 1$) full cell operated in a 17 m $NaClO_4$ electrolyte. We discover that the electrochemical activation through performing electrolytic water oxidation during the formation cycle significantly increases cyclable Na ions intercalated into the $NaTi_2(PO_4)_3$ anode, leading to a specific discharge capacity improvement from 56 to 124 mAh/g for the full cell. Our in-depth synchrotron spectroscopic and imaging studies not only reveal the chemical and structural changes of these electrodes during electrochemical activation but also pinpoint the parasitic cathode−electrolyte interfacial reaction initiated by the electrolytic reaction near the cathode surface, undermining the cell Coulombic efficiency (CE). Further electrochemical measurements uncover that the undesired reactions and products can be modulated by reassembling the cells with the activated electrodes and tuning the cell current density, which is beneficial for fast-charging batteries and potential electrode recycling. This study provides an in-depth, systematic investigation of the interplay between ion intercalation and

https://doi.org/10.1021/acsami.1c19684
ACS Appl. Mater. Interfaces 2022, 14, 12130−12139

Table 1. Hypothesized Electrochemical Reactions during Electrochemical Activation[a]

	cathode	anode
charge	$Na_xFe[Fe(CN)_6] \rightarrow Fe[Fe(CN)_6] + xNa^+ + xe^-$	$NaTi_2(PO_4)_3 + xe^- + xNa^+ \rightarrow Na_{1+x}Ti_2(PO_4)_3$
overcharge	$zH_2O \rightarrow 2zH^+ + z/2O_2 + 2ze^-$	$Na_{1+x}Ti_2(PO_4)_3 + 2zNa^+ + 2ze^- \rightarrow Na_{1+x+2z}Ti_2(PO_4)_3$
discharge	$Fe[Fe(CN)_6] + (x + 2z)Na^+ + (x + 2z)e^- \rightarrow Na_{x+2z}Fe[Fe(CN)_6]$	$Na_{1+x+2z}Ti_2(PO_4)_3 \rightarrow NaTi_2(PO_4)_3 + (x + 2z)Na^+ + (x + 2z)e^-$

[a]This table shows that overcharging can serve as an activation approach to couple ion intercalation and electrolytic reactions. The Na-ion storage in the full cell is increased from x to $x + 2z$ by comparing the pristine cathode and fully discharged cathode, where x represents the original content of Na ions in the pristine NaFeHCF electrode, $2z$ represents the content of introduced Na ions from the electrolyte, and $x + 2z$ is smaller than 2.

electrolytic reactions and elaborates their synergistic effects on the structural and electrochemical properties of ASIBs.

RESULTS AND DISCUSSION

Structural and Electrochemical Characterization of As-Synthesized Electrodes. The as-synthesized Na-deficient $Na_xFe[Fe(CN)_6]$ (NaFeHCF) exhibits a typical face-centered cubic crystal structure with an open frame structure comprising N-coordinated high-spin Fe and C-coordinated low-spin Fe (Figure S1a). The NaFeHCF particles have a cubic morphology with 500−700 nm in size (Figure S1b). The chemical formula of the as-synthesized NaFeHCF is determined to be $Na_{0.94}Fe[Fe(CN)_6]\cdot 2.8H_2O$ through the inductively coupled plasma mass spectrometry (ICP-MS) measurement and thermogravimetric analysis (TGA) (Table S1 and Figure S2). We choose a water-in-salt electrolyte (i.e., 17 m $NaClO_4$) due to its expanded electrochemical stability window allowing for high-voltage charging/discharging of NaFeHCF cathodes. As shown in Figure S3, the electrochemical window of the 17 m $NaClO_4$ electrolyte reaches ∼2.8 V, which is much larger than the theoretical stability window of pure water (∼1.23 V) and allows for complete Na-ion extraction from the NaFeHCF cathode (Figure S4). The cyclic voltammetry (CV) profile of NaFeHCF exhibits characteristic peaks for high-spin (Fe−N) and low-spin (Fe−C) Fe redox couples[24] (Figure S1c), and the galvanostatic charging/discharging shows a specific discharge capacity of 110 mAh/g for the NaFeHCF cathode at 1C (Figure S1d). Based on the charge capacity in the first cycle, the cyclable Na-ion stoichiometry in the as-synthesized NaFeHCF is calculated to be ∼0.75 per chemical formula. Similar measurements conducted on the carbon-coated NTP anode confirm the successful synthesis of $NaTi_2(PO_4)_3$, which exhibits a spherical morphology with a diameter of 100−200 nm and delivers a specific charge capacity of 122 mAh/g at 1C (Figure S5).

Electrochemical Activation of Aqueous Na-Ion Batteries. In aqueous batteries composed of Na-deficient NaFeHCF cathodes and NTP anodes, the amount of cyclable Na ions is intrinsically limited by the Na-ion stoichiometry in as-synthesized PB cathodes, resulting in an inferior specific capacity. We hypothesize that performing electrochemical activation through overcharging can induce electrolytic OER on the NaFeHCF cathode and extra Na-ion intercalation reaction in the NTP anode for the charge compensation. Increasing the cell voltage will thermodynamically enable oxidation on the NaFeHCF cathode and reduction on the NTP anode. The oxidation will start with Na deintercalation from the NaFeHCF lattice, followed by electrolytic OER on the cathode. When the negative potential is higher than the H_2 evolution potential, the reduction will be exclusively limited to Na-ion intercalation in the NTP lattice since there are many Na-ion vacant sites in the as-synthesized NTP. Figure 1a schematically shows such ion intercalation and electrolytic processes. The electrochemical reactions in Table 1 illustrate how such an electrochemical activation method couples both reactions and creates extra cyclable Na ions to participate in the subsequent traditional cell operation (Figure 1b). In other words, theoretically, the Na-deficient NaFeHCF cathode will be electrochemically activated through the coupled reactions and later converted to a Na-rich electrode. Therefore, if successful, the interplay between ion intercalation and electrolytic reactions can boost the capacity and energy density of the ASIB studied here.

To test our hypothesis, the NaFeHCF||NTP full cell is charged with and without electrochemical activation during the first cycle. Figure 1c displays the first charge−discharge curve of the full cell at 1C from 0.2 to 2 V in the 17 m $NaClO_4$ electrolyte, delivering a charge capacity of 64 mAh/g and discharge capacity of 56 mAh/g mainly contributed by the low-spin Fe redox couple. To determine the proper electrochemical activation process in the full cell, we test three different ratios of cathode/anode mass loading and various activation capacities (Figures S6 and S7). Finally, we decided to use a ratio of 1.75 for anode/cathode mass loading and a specific charging capacity of 250 mAh/g for the activation process. Figure 1d shows that, besides the Fe oxidation, a plateau appears at 2.06 V when the full cell is charged to 250 mAh/g in the first charge (i.e., electrochemical activation), which is likely due to electrolytic water oxidation. The initial discharge capacity can reach 124 mAh/g. Meanwhile, the unique discharge plateau around 0.8 V suggests that the high-spin Fe becomes redox active after electrochemical activation, as confirmed by the dQ/dV analysis in Figure S8, where an extra peak corresponding to the high-spin Fe reduction reaction appears in the discharging process. The electrochemically activated full cell shows negligible capacity decay within 100 cycles at 1C after the voltage window is switched to 0.2−2 V (discussed in the Battery Performance of Electrochemically Activated NaFeHCF||NTP Full Cells section).

Realization of Concurrent Ion Intercalation and Electrolytic Reactions. We first employ a transparent two-electrode cell to directly visualize electrolytic reactions (Figure S9) and investigate the electron pathways on both electrodes during electrochemical activation using synchrotron X-ray spectroscopy. Here, we apply Na-free FeHCF (see the Experimental Section for synthesis details) as the cathode to eliminate Fe oxidation so that the charge capacity is solely contributed by electrolytic water oxidation in the first charge of the FeHCF||NTP cell. The CV profile (Figure S10a) and the galvanostatic charging/discharging performance (Figure S10b) of FeHCF exhibit similar features as NaFeHCF materials. We use the same NTP electrode and 17 m $NaClO_4$ as the counter/reference electrode and electrolyte, respectively. After applying the electrochemical activation protocol to this cell, the charging voltage profile exhibits a similar feature as we observe in the coin cell platform, where the high-voltage plateau can be

https://doi.org/10.1021/acsami.1c19684
ACS Appl. Mater. Interfaces 2022, 14, 12130−12139

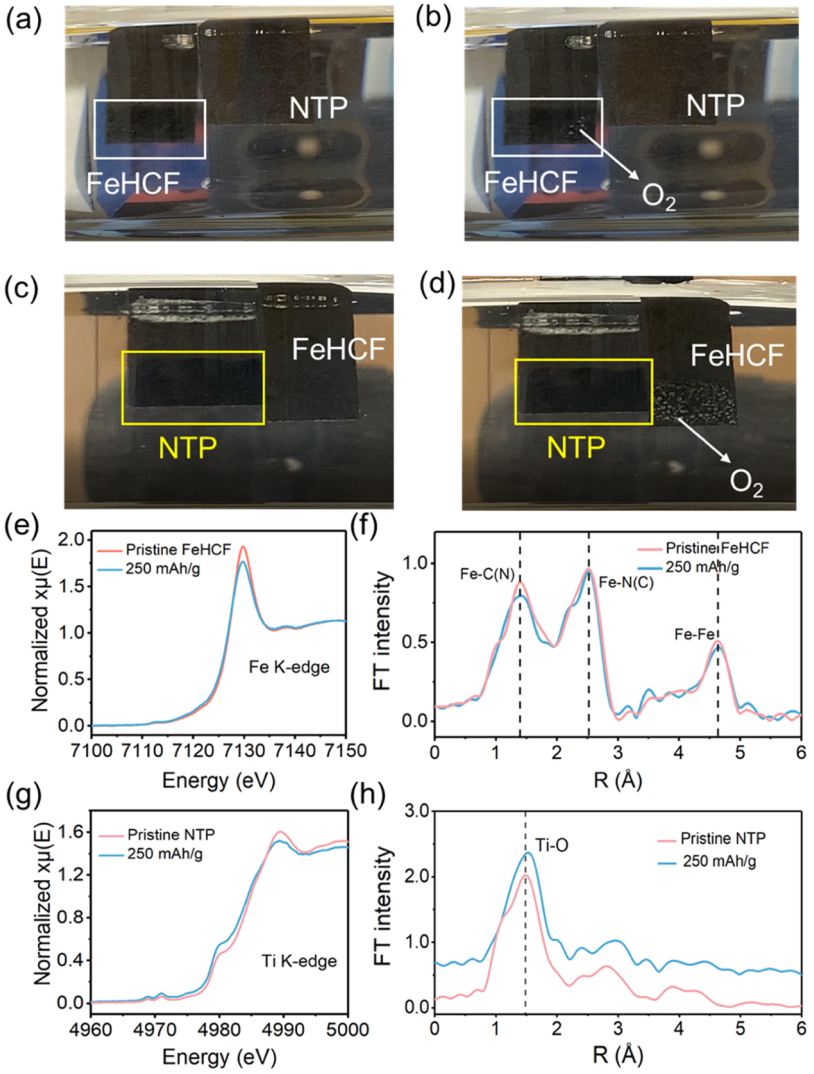

Figure 2. Reaction pathways during electrochemical activation. (a) Appearance of the front side of the FeHCF cathode and the backside of the NTP anode in the pristine state. (b) Appearance of the front side of the FeHCF cathode and the backside of the NTP anode in the electrochemically activated state. (c) Appearance of the backside of the FeHCF cathode and the front side of the NTP anode in the pristine state. (d) Appearance of the backside of the FeHCF cathode and the front side of the NTP anode in the electrochemically activated state. The bubble formation on the cathode confirms the occurrence of OER, while HER is not observed on the NTP anode. The Fe K-edge (e) X-ray absorption near-edge structure (XANES) spectra and (f) extended X-ray absorption fine structure (EXAFS) spectra of the pristine and electrochemically activated FeHCF cathodes. The Ti K-edge (g) XANES spectra and (h) EXAFS spectra of the pristine and electrochemically activated NTP anodes.

assigned to oxygen evolution reaction (Figure S11). The bubble evolution on the electrodes can be tracked using the glassware platform (Supporting Movies 1 and 2). Figure 2a–d shows the snapshots of the pristine and electrochemically activated cells, with regions of interest labeled in the photos. Gas bubbles appear on the front and backsides of the FeHCF cathode upon electrochemical activation (Figure 2b,d), confirming the generation of oxygen gas induced by the electrolytic reaction. In contrast, no gas bubble was observed on either side of the NTP anode upon electrochemical activation, indicating that hydrogen evolution reaction (HER) does not occur on the NTP surface. Therefore, Na-ion intercalation in the anode is required to compensate for the charge neutrality.

We further perform hard X-ray adsorption spectroscopy (XAS) measurements on pristine electrodes and electrodes collected from the electrochemically activated cell. The X-ray absorption near-edge structure (XANES) in Figure 2e reveals that the Fe K-edge energy in the Na-free FeHCF cathode has negligible change after electrochemical activation, indicating that charge capacity is solely contributed by OER. The extended X-ray absorption fine structure (EXAFS) of Fe K-edge (Figure 2f) shows three major peaks around 1.34, 2.42, and 4.60 Å, corresponding to the scattering path of shorter Fe–C (N), longer Fe–N(C), and Fe–Fe shells, respectively. Although the bond length of different shells does not change, the peak intensity of the Fe–C(N) shell declines, which suggests a potential structural distortion of the FeHCF cathode caused by an interfacial electrolytic reaction. Moreover, the edge shift in Ti K-edge XANES spectra (Figure 2g) and elongated Ti–O bond length in Figure 2h imply Ti reduction in the NTP anode after activation, further proving that Na-ion intercalation in the anode is accessible from the electrolyte when cyclable Na ions are absent in the cathode. In summary, we confirm that ion intercalation and electrolytic OER can be triggered simultaneously by the electrochemical activation

https://doi.org/10.1021/acsami.1c19684
ACS Appl. Mater. Interfaces 2022, 14, 12130–12139

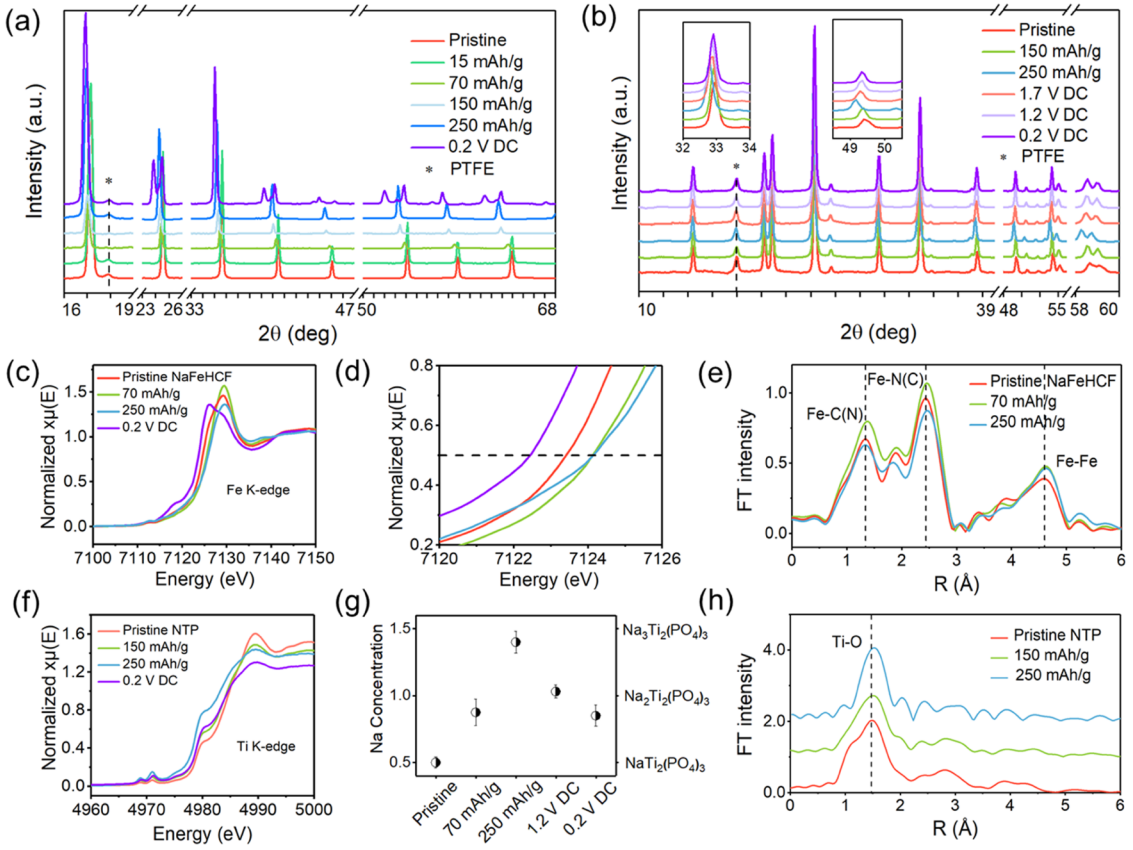

Figure 3. Structural evolution and charge compensation mechanism upon electrochemical activation. (a) Ex situ synchrotron XRD patterns of the NaFeHCF cathode. Normal charging indicates the capacity increasing from pristine to 70 mAh/g, while electrochemical activation indicates the capacity increasing from 70 to 250 mAh/g. DC denotes a state of discharge to different voltages. (b) Ex situ synchrotron XRD patterns of the NTP anode. Reversible lattice expansion and contraction is observed during electrochemical cycling. (c) Fe K-edge XANES spectra of the NaFeHCF cathode at different charging and discharging states. (d) Zoom-in of Fe K-edge XANES spectra. (e) Fourier-transformed magnitude of Fe K-edge EXAFS spectra of the NaFeHCF cathode at pristine and different charging states. (f) Ti K-edge XANES spectra of the NTP anode at different charging and discharging states. The result of 150 mAh/g is close to the result of 0.2 V DC, which suggests that Ti^{3+} is not completely oxidized to Ti^{4+} and there are some residual Na ions in the NTP anode. (g) Na/Ti atomic ratio of the NTP anode during cycling determined by scanning electron microscopy-energy dispersive spectroscopy (SEM-EDS) measurements. The error bars show the standard deviation of four independent measurements. (h) Fourier-transformed magnitude of Ti K-edge EXAFS spectra of the NTP anode at pristine and different charging states.

process, which enables our future investigation regarding the interaction between these two reactions.

Na-Ion Stoichiometry and Structural Changes of Electrodes during Electrochemical Activation. To understand the mechanism underlying the enhanced capacity of NaFeHCF||NTP full cell after electrochemical activation, we use X-ray diffraction (XRD) to measure the structural evolution of both electrodes during the first cycle. As shown in Figure 3a, the cubic phase of the as-synthesized NaFeHCF cathode is converted to a monoclinic phase at the end of discharge, as indicated by the split peaks at 24, 40, and 53°, which implies that the crystal lattice can accommodate more Na ions, resulting in a low-symmetry structure.[28] The XANES results in Figure 3c demonstrate that the Fe in NaFeHCF is oxidized during normal charging (pristine to 70 mAh/g) while exhibits a negligible change in terms of oxidation states upon the electrochemical activation process (70−250 mAh/g). After the first complete cycle, the Fe K-edge of the discharged NaFeHCF ("0.2 V DC") shifts to even lower energy compared to that of the as-synthesized NaFeHCF (Figure 3d), showing that Fe oxidation state is lowered, and the Na-ion stoichiometry is increased in the NaFeHCF cathode in the discharged state. Moreover, the newly appeared shoulder peak at about 7118 eV for the discharged NaFeHCF can be attributed to the 1s to 4p transition followed by ligand-to-metal charge transfer (LMCT), which suggests a strong covalent bonding between Fe ions and CN ligands. Since this pre-edge feature is mostly observed in Na-rich PB materials with low Fe oxidation states,[29] we can speculate that the discharged NaFeHCF cathode has become Na-rich. The ICP results in Table S2 show that the NaFeHCF becomes nearly Na-free ($Na_{0.13}Fe[Fe(CN)_6]$) after the first activation process and then converts to Na-rich ($Na_{1.78}Fe[Fe(CN)_6]$) at the fully discharged state, confirming our previous conclusion.

The NTP anode experiences solid-solution reactions in the first cycle. The lattice structure exhibits a typical expansion−contraction behavior upon sodiation−desodiation (Figure 3b), suggesting a reversible redox reaction in the anode. Similar to the results we obtained from the transparent two-electrode cell (Figure 2g,h), the continuous Ti K-edge shift (Figure 3f) and gradually increased Ti−O bond length (Figure 3h) uncover that Na-ion intercalation takes place in the NTP anode throughout the charging process of the full cell. Furthermore, energy-dispersive X-ray spectroscopy (EDS) measurements reveal the Na/Ti atomic ratio of NTP anodes at different states of charge (SOCs) and discharge. Four regions are measured

https://doi.org/10.1021/acsami.1c19684
ACS Appl. Mater. Interfaces 2022, 14, 12130−12139

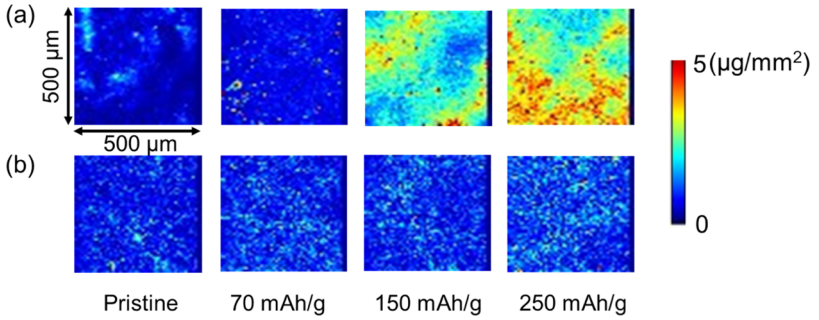

Figure 4. Transition-metal dissolution upon electrochemical activation. The evolution of (a) Fe and (b) Ti dissolution and deposition on separators upon charging and electrochemical activation process determined by X-ray fluorescence microscopy measurements. These images suggest that some Fe species in NaFeHCF is dissolved upon electrochemical activation, whereas Ti species in NTP remains stable during electrochemical cycling.

for each electrode using SEM-EDS, and the averaged results are summarized in Figure 3g. The Na/Ti atomic ratio keeps increasing upon cell normal charging and electrochemical activation, which directly shows that the Na-ion is intercalated to the NTP anode to complete the full cell reaction. The higher Na/Ti atomic ratio at the cell discharged state compared to the as-synthesized NTP presents that there are still excess Na ions stored in the NTP anode. The ICP results in Table S3 demonstrate a similar Na/Ti ratio with EDS data and confirm the behavior of Na-ion in the NTP anode. The NaFeHCF cathode has run out of cyclable Na ions after 70 mAh/g in the first charging of the NaFeHCF||NTP full cell; thus, additional Na ions can only be acquired from the aqueous electrolyte. The Na-ion concentration in the electrolyte is 17 m, which is well beyond the critical "WIS" criterion (8.19 m). Therefore, such additional Na-ion intercalation would show a negligible impact on the electrolyte concentration and the electrolyte voltage stability window. In summary, we conclude that the interplay between ion intercalation and electrolytic reactions can increase the Na-ion storage and be beneficial for ASIBs with inadequate Na-ion inventory.

Interfacial Parasitic Reactions Initiated by Electrochemical Activation. Although the combined reactions grant higher Na-ion inventory in the full cell configuration, redox reactions during electrochemical activation are more complicated due to the presence of interfacial parasitic reactions. Investigating the side effects can complement the understanding of the electrochemical activation process. For the NaFeHCF cathode, the XRD and XANES results show that, during the electrochemical activation (from 70 to 250 mAh/g in the first charge), although the oxidation state of Fe is unchanged (Figure 3d), crystal lattice exhibits expansion behavior (Figure 3a). Considering that OER generates protons near the electrode surface (Figure 1a and Table 1) and builds up an acidic environment across the cathode−electrolyte interface, we conjecture that lattice variation is mediated by OER. Compared to the Na-free FeHCF, the EXAFS results of pristine NaFeHCF (Figure 3e) show a similar local structure surrounding Fe atoms except for a new peak located at 1.9 Å, which has been observed in other PB materials[29,30] and is likely associated with the twisted local structure surrounding the central Fe atom owing to the existence of Na ions in NaFeHCF. The fact that such feature remains at charged state indicates that there are still some residual Na ions presenting in the lattice structure, and further comparison regarding the Fe oxidation state between charged NaFeHCF and as-prepared Na-free FeHCF reference supports our speculation (Figure S12). After the electrochemical activation process (250 mAh/g), the intensity of Fe−C and Fe−N peaks decreases. This result implies that, as previously reported,[31,32] the $[Fe(CN)_6]^{3-/4-}$ group in PB materials is sensitive to the pH value in the solution and can potentially dissolve into electrolytes during OER, leading to the variation of the chemical and structural environment surrounding Fe atoms.

Therefore, we further perform synchrotron X-ray fluorescence microscopy (XFM) on battery separators to quantify transition-metal dissolution from the electrodes and investigate the interfacial parasitic reaction. We collect separators from battery cells at different states of charge (SOCs) to investigate Fe and Ti dissolution. Upon charging the cell to 70 mAh/g, both cathode and anode show no discernable transition-metal dissolution (Figure 4). However, upon electrochemical activation, Fe in the NaFeHCF cathode undergoes more severe dissolution (Figure 4a), whereas Ti in the NTP anode is more stable (Figure 4b). The areal concentration of dissolved Fe species is determined to be 3.78 ± 1.52 $\mu g/mm^2$ after the complete electrochemical activation to 250 mAh/g. Moreover, transmission electron microscopy (TEM) images show the evolution of the NaFeHCF particle morphology after electrochemical activation (Figure S13). The particles transform from cubic-shaped crystals in the as-synthesized state to irregular-shaped crystals after electrochemical activation, which is associated with the Fe dissolution behavior. The EXAFS results together with XFM and TEM analysis confirm the occurrence of Fe loss and accompanied structural and morphological variation induced by the electrolytic reactions.

Battery Performance of Electrochemically Activated NaFeHCF||NTP Full Cells. Figure S14a,b exhibits the battery performance of NaFeHCF||NTP full cells with normal charging protocol and with electrochemical activation in the first charge, respectively. The cell without electrochemical activation delivers inferior discharge capacity but retains good CE (~98%) during the first 100 cycles at 1C. In comparison, the cell with electrochemical activation shows significantly improved discharge capacity (110 mAh/g @ second cycle) and a 98% capacity retention within 100 cycles at 1C. Note that sufficient ion intercalation reactions introduce excess Na ions into the NTP anode; thus, it can potentially serve as a Na-ion reservoir to compensate the Na loss during electrochemical cycling, which promotes a more stable performance. However, the CE drops to ~90% in the electrochemically activated cell, indicating that, as we expected, oxygen molecules accompanied by Fe dissolution on the cathode lead to cycling irreversibility.

https://doi.org/10.1021/acsami.1c19684
ACS Appl. Mater. Interfaces 2022, 14, 12130−12139

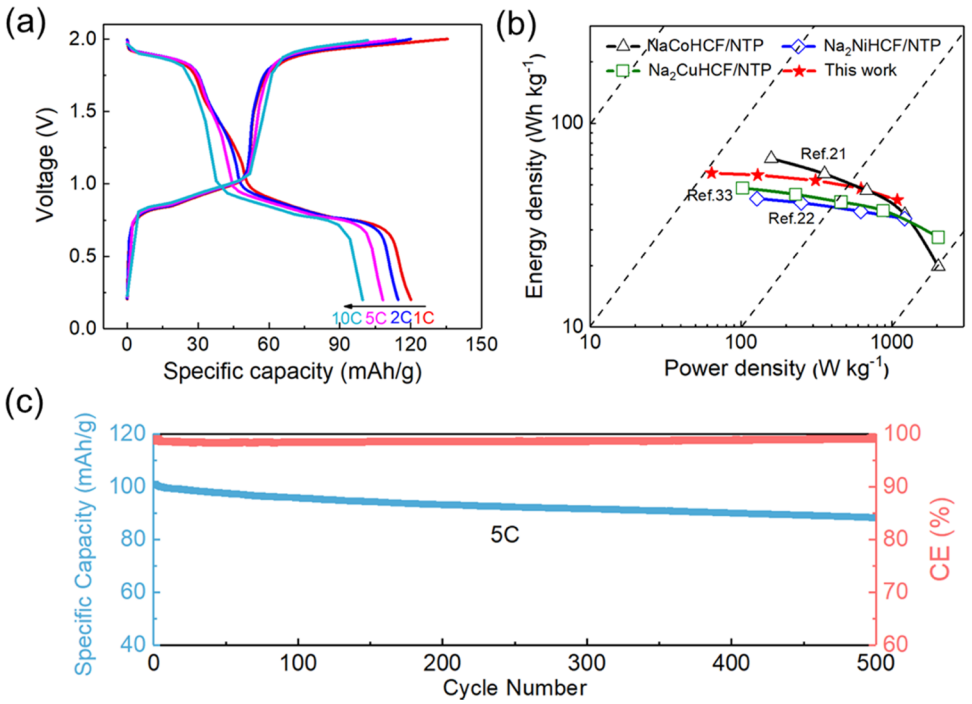

Figure 5. Performance of the electrochemically activated NaFeHCF||NTP full cell. (a) Typical charge−discharge curves between 0.2 and 2.0 V of the full cell at 1C, 2C, 5C, and 10C rates. (b) Ragonne plot shows the comparison of output specific power and energy for the full cell with reported Na-rich PB||NTP aqueous full cells; the energy and power densities of full cells are calculated based on the total mass of the active cathode and anode. (c) Long-term cycling performance of the reassembled NaFeHCF||NTP full cell at 5C. The fresh cell is disassembled after one complete electrochemical activation cycle. The electrodes are collected and used in the reassembled NaFeHCF||NTP full cell. The capacity calculation is based on the mass of an active cathode. The voltage is set to 0.2−1.9 V to avoid potential OER. 1C is defined as 170 mA/g.

The electrochemically activated NaFeHCF||NTP full cell displays a good rate capability (Figure 5a). Specifically, the cell delivers a discharge capacity of ∼120 mAh/g-cathode at 1C from 0.2 to 2 V and still retains 101 mAh/g at 10C, with a high CE of ∼99%. The Ragonne plots (Figure 5b) show that the electrochemically activated NaFeHCF||NTP cell is on par with the performance that the literature has demonstrated for Na-rich PB||NTP systems.[21,22,33] Specifically, the NaFeHCF||NTP full cell delivers a specific energy of 57 Wh/kg at a specific power of 64 W/kg and still maintains a specific energy of 48 Wh/kg at a specific power of 626 W/kg.

To mitigate the low CE in electrochemically activated cells caused by the generated oxygen and dissolved Fe species, we disassemble the coin cell after the first activation cycle and reassemble another fresh cell using the same cathode and anode. We further limit the voltage range to 0.2−1.9 V to avoid undesired OER at high charging potentials, which also slightly reduces the specific capacity of NaFeHCF materials because the low-spin Fe is not completely oxidized within such voltage range. Figure S15 shows that the CE is enhanced to ∼97% at 1C in the reassembled cell. Moreover, as shown in Figure 5c, the reassembled cell demonstrates good cycle life, with an initial capacity of 102 mAh/g at 5C and a capacity retention of 87.6% after 500 cycles, which is comparable with the cycling stability of other Na-rich PB-based full cell systems (Table S4). Since no extra interphase is detected on the electrochemically activated NTP surface (Figure S16), combined with the negligible change in terms of C 1s and P 2p peaks in pristine and activated NTP according to the X-ray photoelectron spectroscopy (XPS) results in Figure S17, we believe that no new interphase is formed after the first cycle. Therefore, we think that the improved CE and good cycle life of the reassembled cell results from the inhibited side reactions. On the other hand, the activation process can be treated as a one-time processing approach to manipulating the Na-ion storage in Na-poor PB materials. The obtained electrodes can be further utilized in other cell assemblies, which will deliver better electrochemical performance. Moreover, it will be more valuable to apply an activation approach to recycle the PB materials. For example, Na-rich PB materials will inevitably experience the Na-ion inventory loss after long-time cycling, especially in the full cell configuration. If the structure maintains stability, the activation process can enrich the Na-ion content and make the electrodes functionalized again. In summary, the interplay between ion intercalation and electrolytic reactions serves as an *in situ* electrochemical approach to synthesize Na-rich PB materials and enables improved performance, which is more meaningful in fast-charging, electrode-recycling applications.

CONCLUSIONS

Understanding and tailoring ion intercalation and electrolytic reactions is a long-standing scientific challenge in the development of advanced aqueous batteries. At the single electrode level, electrolytic reactions might compete with ion intercalation reactions, which negatively impact battery performance such as capacity and cycle life. In this study, we perform OER electrolytic reaction and Na-ion intercalation simultaneously in a full cell ASIB, as an electrochemical activation approach to investigate the interplay between these two distinct reactions. Through systematic chemical, structural, and electrochemical analyses, we conclude that such an electrochemical activation method can effectively mitigate the ion inventory issue in full cell batteries, especially those based

https://doi.org/10.1021/acsami.1c19684
ACS Appl. Mater. Interfaces 2022, 14, 12130−12139

on high-concentration electrolytes, such as water-in-salt electrolytes. Specifically, in our Na-deficient NaFeHCF||NTP platform, charging NaFeHCF beyond the Na-ion deintercalation potential leads to electrolytic water oxidation on the desodiated NaFeHCF electrode. Meanwhile, Na-ion intercalation takes place in the NTP anode, with Na ions desolvated from the electrolyte. This electrochemical activation significantly increases cyclable Na ions in the full cell, resulting in a significant boost of initial specific discharge capacity from 56 to 124 mAh/g. We also recognize that the interfacial electrolytic process may compromise the stability of electrode materials. For example, the acidic environment created at the cathode−electrolyte interface during electrolytic reactions may distort the lattice structure of cathode and promote Fe dissolution. These parasitic side reactions can be inhibited by reassembling the cell after the electrochemical activation process, which enables improved cycle life and Coulombic efficiency. We expect that in alkali battery cells where slight decomposition of the electrolyte is not a concern, such as the water-in-salt electrolyte studied herein, the electrochemical activation protocol can be applied to resolve the challenges surrounding ion loss in alkali ion batteries. For practical aqueous batteries, since they can be assembled easily in the open-air condition, the generated oxygen gas may be vented after electrochemical activation in the first cycle or captured by oxygen scavengers in the cell. Moreover, this activation approach might serve as a recycling approach to enrich the Na-ion inventory for the electrodes that undergo severe Na-ion loss after long-time cycling. The reactivated electrodes can be further utilized in other cell assemblies and deliver satisfying performance. In summary, this study creates fundamental insights into the interplay between ion intercalation and electrolytic OER in ASIBs and systematically investigates their impacts on the structural evolution of electrodes and the electrochemical performance of full cells, potentially providing a strategy to manipulate ion inventory in aqueous batteries.

EXPERIMENTAL SECTION

Material Synthesis. $Na_xFe[Fe(CN)_6]$ (NaFeHCF) was synthesized through a coprecipitation method. First, 0.75 g of carbon black powder was added to 100 mL of deionized water and sonicated for 2 h to obtain a homogeneous solution. Then, 10 mmol $Na_4[Fe(CN)_6]$ and 1 mL of concentrated hydrochloric acid were dissolved in the as-prepared solution. The mixture was continuously stirred at 60 °C for 8 h. Finally, the composite was washed three times with deionized water, filtered, and dried in the vacuum oven at 120 °C for 12 h. The Na-free FeHCF was synthesized using $K_3[Fe(CN)_6]$ as a single ion source. Typically, 10 mmol $K_3[Fe(CN)_6]$ and 1 mL of concentrated hydrochloric acid were added to 100 mL of deionized water. Then, the mixture was heated at 60 °C for 8 h under vigorous stirring. The precipitates were washed three times with deionized water, filtered, and dried at 120 °C for 12 h to obtain the FeHCF product. NTP material was synthesized through the solid-state method. First, stoichiometric amounts of $NH_4H_2PO_4$, Na_2CO_3, and TiO_2 were ball-milled with acetone at a rate of 500 rpm for 8 h. The mixed precursors were dried in the vacuum oven at 60 °C for 12 h and heated at 900 °C for 24 h in a box furnace. The product was mixed with sucrose, ball-milled at a rate of 500 rpm for 2 h, and calcined in the tube furnace at 850 °C for 2 h to obtain the final $NaTi_2(PO_4)_3$/C product.

Electrochemical Measurements. To prepare composite electrodes for three-electrode measurements, poly(vinylidene difluoride (PVDF), as the binder) was first dissolved into *N*-methyl-2-pyrrolidone, and then the active material (NaFeHCF or NTP) and acetylene carbon were added into the solution and thoroughly mixed, following the weight ratio of active material/PVDF/acetylene carbon = 8:1:1. The electrode slurry was drop casted onto the carbon paper (Toray Carbon Paper 090, The Fuel Cell Store) and dried in air. The aqueous electrolyte used here was 17 m $NaClO_4$, which was prepared by dissolving 17 mol $NaClO_4$ salt in 1 L of water. The three-electrode cell was constructed using the NaFeHCF composite (3.2 mg/cm^2) or NTP composite (3.6 mg/cm^2) electrode as the working electrode, Pt foil as the counter electrode, and saturated calomel electrode (SCE) as the reference electrode. The transparent two-electrode cell contains FeHCF as the working electrode (3.2 mg/cm^2) and NTP (3.6 mg/cm^2) as the counter/reference electrode. The mass ratio of FeHCF/NTP is 1:1.9 by controlling the area of electrodes. Both cyclic voltammetry (CV) and galvanostatic cycling with potential limitation (GCPL) measurements were conducted on a potentiostat (SP-150, Biologic, France). The electrolytes were purged with N_2 overnight before testing to eliminate the dissolved oxygen. To prepare composite electrodes for full cell testing, poly(tetrafluoroethylene) (PTFE) was thoroughly mixed with active materials (NaFeHCF or NTP) and acetylene black, following the weight ratio of active material/PTFE/acetylene black = 8:1:1. The mixture was compressed on a stainless-steel grid. The fabricated electrodes were used as cathodes and anodes, separately, with the Whatman glass fiber (1827-047934-AH) as the separator. The full aqueous Na-ion cells were assembled in CR2032-type coin cells and galvanostatically charged/discharged on electrochemical workstations (Wuhan Land Company). The mass ratio of NaFeHCF/NTP is 1:1.75, the mass loading of NaFeHCF is 3.2 mg/cm^2, and the mass loading of NTP is 4.5 mg/cm^2. To evaluate the energy density, power density, and cycle life of fully activated cell, the cycled electrodes were collected to reassemble the cell and the mass ratio of NaFeHCF/NTP is 1:1.25, corresponding to a capacity ratio of 1:1.35. 1C corresponds to a specific current rate of 170 mA/g.

Characterization of Materials. The morphology of the materials was characterized on an LEO 1550 field-emission scanning electron microscope (SEM) with an accelerating voltage of 6 kV. EDS measurements were carried out with the SEM with an accelerating voltage of 20 kV. The lab X-ray diffraction (XRD) results were obtained on a Rigaku Miniflex II diffractometer with a Cu Kα X-ray radiation (λ = 1.54 Å) in a scan range of 10−60°. ICP-MS measurements were performed on a Thermo Electron ICAP-RQ spectrometer (Thermo Fisher). TEM images were acquired from a JOEL 2100 Cryo transmission electron microscope at an acceleration voltage of 200 kV. The synchrotron XRD patterns were collected at the beamline 11-3 of SSRL at SLAC National Accelerator Laboratory with an X-ray wavelength of 0.9762 Å. A LaB_6 sample was used to calibrate the diffraction configuration. The XRD patterns were converted to the Cu Kα-based XRD with a wavelength of 1.5406 Å. The hard XAS measurements were carried out at beamline 7-BM (QAS) of the NSLS-II at Brookhaven National Laboratory, except for the data collected for ex situ NaFeHCF in Figure 3c−e, which were collected at beamline 20-ID at the Advanced Photon Source, Argonne National Laboratory. Both the Fe and Ti K-edge spectra were collected in the fluorescence mode, with the samples aligned at an angle of ∼45° with respect to the incident beam and the Lytle detector. The XANES and EXAFS data were analyzed with ATHENA software. The energy calibration was carried out using the first inflection point of the Ti or Fe K-edge spectra of the transition-metal foil as a reference. The samples for hard XAS and synchrotron XRD were sealed with Kapton tapes and stored in an Ar-filled glovebox before measurements. XFM measurements were conducted at the 2-ID-E beamline at the Advanced Photon Source, Argonne National Laboratory. The samples were raster-scanned by a sub-micrometer focused 10 keV X-ray beam with a step size of 10 μm. The fluorescent X-rays were detected with a four-element silicon-drift Vortex detector, and the raw data were processed and quantified with MAPS.

ASSOCIATED CONTENT

Supporting Information

The Supporting Information is available free of charge at https://pubs.acs.org/doi/10.1021/acsami.1c19684.

https://doi.org/10.1021/acsami.1c19684
ACS Appl. Mater. Interfaces 2022, 14, 12130−12139

Bubble evolution on the front side of FeHCF cathode (left region of the video) and back side of NTP anode (right region of the video) during electrochemical charging (activation) process; bubble formation is observed only on the front side of FeHCF cathode (MP4)

Bubble evolution on the back side of FeHCF cathode (right region of the video) and front side of NTP anode (left region of the video) during electrochemical charging (activation) process; bubble formation is observed only on the back side of FeHCF cathode (MP4)

SEM images, XRD patterns, and CV and GCPL performances of NaFeHCF; TGA analysis of NaFeHCF; the stability window of 17 m $NaClO_4$ electrolyte; SEM images, XRD patterns, and CV and GCPL performances of NTP; full cell performance using different concentrations of $NaClO_4$ electrolytes; full cell performance with different NaFeHCF/NTP mass ratios and different activation capacities; schematic illustration of a two-electrode glassware cell; CV and GCPL performance of FeHCF; charge−discharge curve of a FeHCF||NTP two-electrode cell; XANES spectra of FeHCF; TEM images of pristine and activated NTP; long-term electrochemical performance of the full cells with and without the activation step; the electrochemical performance of reassembled full cell; XPS results of pristine and cycled NTP; ICP results of pristine NaFeHCF; ICP results of NaFeHCF at different charge/discharge states; ICP results of NTP at different charge/discharge states; the electrochemical cycle life of Na-rich PB-based aqueous Na-ion batteries reported in the literature; and bubble evolution in the two-electrode glassware system (PDF)

AUTHOR INFORMATION

Corresponding Author

Feng Lin − *Department of Chemistry, Virginia Tech, Blacksburg, Virginia 24073, United States;* orcid.org/0000-0002-3729-3148; Email: fenglin@vt.edu

Authors

Yuxin Zhang − *Department of Chemistry, Virginia Tech, Blacksburg, Virginia 24073, United States;* orcid.org/0000-0002-2830-4159

Chunguang Kuai − *Department of Chemistry, Virginia Tech, Blacksburg, Virginia 24073, United States*

Anyang Hu − *Department of Chemistry, Virginia Tech, Blacksburg, Virginia 24073, United States;* orcid.org/0000-0003-0669-9126

Lu Ma − *National Synchrotron Light Source II, Brookhaven National Laboratory, Upton, New York 11973, United States*

Sha Tan − *Chemistry Division, Brookhaven National Laboratory, Upton, New York 11973, United States*

Inhui Hwang − *Advanced Photon Source, Argonne National Laboratory, Lemont, Illinois 60439, United States*

Linqin Mu − *Department of Chemistry, Virginia Tech, Blacksburg, Virginia 24073, United States;* orcid.org/0000-0003-4421-4820

Muhammad Mominur Rahman − *Department of Chemistry, Virginia Tech, Blacksburg, Virginia 24073, United States;* orcid.org/0000-0001-6814-456X

Cheng-Jun Sun − *Advanced Photon Source, Argonne National Laboratory, Lemont, Illinois 60439, United States*

Luxi Li − *Advanced Photon Source, Argonne National Laboratory, Lemont, Illinois 60439, United States*

Enyuan Hu − *Chemistry Division, Brookhaven National Laboratory, Upton, New York 11973, United States;* orcid.org/0000-0002-1881-4534

Complete contact information is available at: https://pubs.acs.org/10.1021/acsami.1c19684

Author Contributions

F.L. conceived and led the project. Y.Z. and F.L. designed experiments. Y.Z. performed material synthesis, characterization, and electrochemical experiments. L.M., S.T., E.H., I.H., and C.-J.S. performed hard XAS. A.H. performed lab XRD and SEM-EDS. L.M. performed TEM. L.L. performed XFM. C.K. and M.M.R. performed synchrotron XRD. Y.Z. and F.L. wrote the manuscript with the help of all co-authors.

Notes

The authors declare no competing financial interest.

ACKNOWLEDGMENTS

The project was supported by the National Science Foundation (No. CBET-1912885). The use of the Stanford Synchrotron Radiation Light source, SLAC National Accelerator Laboratory, was supported by the U.S. Department of Energy, Office of Science, Office of Basic Energy Sciences under Contract no. DE-AC02-76SF00515. S.T. and E.H. at Brookhaven National Laboratory (BNL) were supported by the Assistant Secretary for Energy Efficiency and Renewable Energy, Vehicle Technology Office of the U.S. Department of Energy through the Advanced Battery Materials Research (BMR) Program, under contract DE-SC0012704. This research used resources of the Advanced Photon Source, a U.S. Department of Energy (DOE) Office of Science User Facility operated for the DOE Office of Science by Argonne National Laboratory under Contract no. DE-AC02-06CH11357.

REFERENCES

(1) Jin, T.; Wang, P.; Wang, Q.; Zhu, K.; Deng, T.; Zhang, J.; Zhang, W.; Yang, X.; Jiao, L.; Wang, C. Realizing Complete Solid-Solution Reaction in High Sodium Content P2-Type Cathode for High-Performance Sodium-Ion Batteries. *Angew. Chem.* **2020**, *132*, 14619−14624.

(2) Lee, M.; Hong, J.; Lopez, J.; Sun, Y.; Feng, D.; Lim, K.; Chueh, W. C.; Toney, M. F.; Cui, Y.; Bao, Z. High-Performance Sodium−Organic Battery by Realizing Four-Sodium Storage in Disodium Rhodizonate. *Nat. Energy* **2017**, *2*, 861−868.

(3) Zhu, Y.; Wen, Y.; Fan, X.; Gao, T.; Han, F.; Luo, C.; Liou, S.-C.; Wang, C. Red Phosphorus−Single-Walled Carbon Nanotube Composite as a Superior Anode for Sodium Ion Batteries. *ACS Nano* **2015**, *9*, 3254−3264.

(4) Suo, L.; Borodin, O.; Wang, Y.; Rong, X.; Sun, W.; Fan, X.; Xu, S.; Schroeder, M. A.; Cresce, A. V.; Wang, F.; et al. "Water-in-Salt" Electrolyte Makes Aqueous Sodium-Ion Battery Safe, Green, and Long-Lasting. *Adv. Energy Mater.* **2017**, *7*, No. 1701189.

(5) Kühnel, R.; Reber, D.; Battaglia, C. A High-Voltage Aqueous Electrolyte for Sodium-Ion Batteries. *ACS Energy Lett.* **2017**, *2*, 2005−2006.

(6) Nakamoto, K.; Sakamoto, R.; Ito, M.; Kitajou, A.; Okada, S. Effect of Concentrated Electrolyte on Aqueous Sodium-Ion Battery with Sodium Manganese Hexacyanoferrate Cathode. *Electrochemistry* **2017**, *85*, 179−185.

(7) Luo, J.-Y.; Cui, W.-J.; He, P.; Xia, Y.-Y. Raising the Cycling Stability of Aqueous Lithium-Ion Batteries by Eliminating Oxygen in the Electrolyte. *Nat. Chem.* **2010**, *2*, 760−765.
(8) Lee, M. H.; Kim, S. J.; Chang, D.; Kim, J.; Moon, S.; Oh, K.; Park, K.-Y.; Seong, W. M.; Park, H.; Kwon, G.; et al. Toward a Low-Cost High-Voltage Sodium Aqueous Rechargeable Battery. *Mater. Today* **2019**, *29*, 26−36.
(9) Jiang, L.; Liu, L.; Yue, J.; Zhang, Q.; Zhou, A.; Borodin, O.; Suo, L.; Li, H.; Chen, L.; Xu, K.; Hu, Y.-S. High-Voltage Aqueous Na-Ion Battery Enabled by Inert-Cation-Assisted Water-in-Salt Electrolyte. *Adv. Mater.* **2020**, *32*, No. 1904427.
(10) Nakamoto, K.; Sakamoto, R.; Sawada, Y.; Ito, M.; Okada, S. Over 2 V Aqueous Sodium-Ion Battery with Prussian Blue-Type Electrodes. *Small Methods* **2019**, *3*, No. 1800220.
(11) Zheng, Q.; Miura, S.; Miyazaki, K.; Ko, S.; Watanabe, E.; Okoshi, M.; Chou, C.; Nishimura, Y.; Nakai, H.; Kamiya, T.; et al. Sodium-and Potassium-Hydrate Melts Containing Asymmetric Imide Anions for High-Voltage Aqueous Batteries. *Angew. Chem., Int. Ed.* **2019**, *58*, 14202−14207.
(12) Reber, D.; Kühnel, R.-S.; Battaglia, C. Suppressing Crystallization of Water-in-Salt Electrolytes by Asymmetric Anions Enables Low-Temperature Operation of High-Voltage Aqueous Batteries. *ACS Mater. Lett.* **2019**, *1*, 44−51.
(13) Ling, Y.; Wang, G.; Reddy, J.; Wang, C.; Zhang, J. Z.; Li, Y. The Influence of Oxygen Content on the Thermal Activation of Hematite Nanowires. *Angew. Chem.* **2012**, *124*, 4150−4155.
(14) Cheng, Y.; Zhang, H.; Lu, S.; Varanasi, C. V.; Liu, J. Flexible Asymmetric Supercapacitors with High Energy and High Power Density in Aqueous Electrolytes. *Nanoscale* **2013**, *5*, 1067−1073.
(15) Yang, P.; Ding, Y.; Lin, Z.; Chen, Z.; Li, Y.; Qiang, P.; Ebrahimi, M.; Mai, W.; Wong, C. P.; Wang, Z. L. Low-Cost High-Performance Solid-State Asymmetric Supercapacitors Based on MnO_2 Nanowires and Fe_2O_3 Nanotubes. *Nano Lett.* **2014**, *14*, 731−736.
(16) Lu, X.; Yu, M.; Wang, G.; Zhai, T.; Xie, S.; Ling, Y.; Tong, Y.; Li, Y. H-TiO_2@ MnO_2//H-TiO_2@ C Core−Shell Nanowires for High Performance and Flexible Asymmetric Supercapacitors. *Adv. Mater.* **2013**, *25*, 267−272.
(17) Jabeen, N.; Xia, Q.; Savilov, S. V.; Aldoshin, S. M.; Yu, Y.; Xia, H. Enhanced Pseudocapacitive Performance of α-MnO_2 by Cation Preinsertion. *ACS Appl. Mater. Interfaces* **2016**, *8*, 33732−33740.
(18) Jabeen, N.; Hussain, A.; Xia, Q.; Sun, S.; Zhu, J.; Xia, H. High-performance 2.6 V Aqueous Asymmetric Supercapacitors Based on in Situ Formed $Na_{0.5}MnO_2$ Nanosheet Assembled Nanowall Arrays. *Adv. Mater.* **2017**, *29*, No. 1700804.
(19) Sarasketa-Zabala, E.; Aguesse, F.; Villarreal, I.; Rodriguez-Martinez, L. M.; López, C. M.; Kubiak, P. Understanding Lithium Inventory Loss and Sudden Performance Fade in Cylindrical Cells during Cycling with Deep-Discharge Steps. *J. Phys. Chem. C* **2015**, *119*, 896−906.
(20) Birkl, C. R.; Roberts, M. R.; McTurk, E.; Bruce, P. G.; Howey, D. A. Degradation Diagnostics for Lithium Ion Cells. *J. Power Sources* **2017**, *341*, 373−386.
(21) Wu, X.; Sun, M.; Guo, S.; Qian, J.; Liu, Y.; Cao, Y.; Ai, X.; Yang, H. Vacancy-Free Prussian Blue Nanocrystals with High Capacity and Superior Cyclability for Aqueous Sodium-Ion Batteries. *ChemNanoMat* **2015**, *1*, 188−193.
(22) Wu, X.; Cao, Y.; Ai, X.; Qian, J.; Yang, H. A Low-Cost and Environmentally Benign Aqueous Rechargeable Sodium-Ion Battery Based on $NaTi_2(PO_4)_3$−$Na_2NiFe(CN)_6$ Intercalation Chemistry. *Electrochem. Commun.* **2013**, *31*, 145−148.
(23) Li, Z.; Young, D.; Xiang, K.; Carter, W. C.; Chiang, Y. Towards High Power High Energy Aqueous Sodium-ion Batteries: The $NaTi_2(PO_4)_3$/$Na_{0.44}MnO_2$ System. *Adv. Energy Mater.* **2013**, *3*, 290−294.
(24) Wu, X.; Luo, Y.; Sun, M.; Qian, J.; Cao, Y.; Ai, X.; Yang, H. Low-Defect Prussian Blue Nanocubes as High Capacity and Long Life Cathodes for Aqueous Na-Ion Batteries. *Nano Energy* **2015**, *13*, 117−123.
(25) You, Y.; Wu, X.-L.; Yin, Y.-X.; Guo, Y.-G. High-Quality Prussian Blue Crystals as Superior Cathode Materials for Room-Temperature Sodium-Ion Batteries. *Energy Environ. Sci.* **2014**, *7*, 1643−1647.
(26) Yang, Y.; Liu, E.; Yan, X.; Ma, C.; Wen, W.; Liao, X.-Z.; Ma, Z.-F. Influence of Structural Imperfection on Electrochemical Behavior of Prussian Blue Cathode Materials for Sodium Ion Batteries. *J. Electrochem. Soc.* **2016**, *163*, A2117−A2123.
(27) Wang, W.; Gang, Y.; Hu, Z.; Yan, Z.; Li, W.; Li, Y.; Gu, Q.-F.; Wang, Z.; Chou, S.-L.; Liu, H.-K.; Dou, S.-X. Reversible Structural Evolution of Sodium-Rich Rhombohedral Prussian Blue for Sodium-Ion Batteries. *Nat. Commun.* **2020**, *11*, No. 980.
(28) Song, J.; Wang, L.; Lu, Y.; Liu, J.; Guo, B.; Xiao, P.; Lee, J.-J.; Yang, X.-Q.; Henkelman, G.; Goodenough, J. B. Removal of Interstitial H_2O in Hexacyanometallates for a Superior Cathode of a Sodium-Ion Battery. *J. Am. Chem. Soc.* **2015**, *137*, 2658−2664.
(29) You, Y.; Yu, X.; Yin, Y.; Nam, K.-W.; Guo, Y.-G. Sodium Iron Hexacyanoferrate with High Na Content as a Na-Rich Cathode Material for Na-Ion Batteries. *Nano Res.* **2015**, *8*, 117−128.
(30) Xie, B.; Zuo, P.; Wang, L.; Wang, J.; Huo, H.; He, M.; Shu, J.; Li, H.; Lou, S.; Yin, G. Achieving Long-Life Prussian Blue Analogue Cathode for Na-Ion Batteries via Triple-Cation Lattice Substitution and Coordinated Water Capture. *Nano Energy* **2019**, *61*, 201−210.
(31) Yu, Z.-Y.; Duan, Y.; Liu, J.-D.; Chen, Y.; Liu, X.-K.; Liu, W.; Ma, T.; Li, Y.; Zheng, X.-S.; Yao, T.; et al. Unconventional CN Vacancies Suppress Iron-Leaching in Prussian Blue Analogue Pre-Catalyst for Boosted Oxygen Evolution Catalysis. *Nat. Commun.* **2019**, *10*, No. 2799.
(32) Han, L.; Tang, P.; Reyes-Carmona, A.; Rodríguez-García, B.; Torréns, M.; Morante, J. R.; Arbiol, J.; Galan-Mascaros, J. R. Enhanced Activity and Acid PH Stability of Prussian Blue-Type Oxygen Evolution Electrocatalysts Processed by Chemical Etching. *J. Am. Chem. Soc.* **2016**, *138*, 16037−16045.
(33) Wu, X.; Sun, M.; Shen, Y.; Qian, J.; Cao, Y.; Ai, X.; Yang, H. Energetic Aqueous Rechargeable Sodium-Ion Battery Based on $Na_2CuFe(CN)_6$−$NaTi_2(PO4)_3$ Intercalation Chemistry. *ChemSusChem* **2014**, *7*, 407−411.

https://doi.org/10.1021/acsami.1c19684
ACS Appl. Mater. Interfaces 2022, 14, 12130−12139